remote sensing

Article

Coastal Reclamation Embankment Deformation: Dynamic Monitoring and Future Trend Prediction Using Multi-Temporal InSAR Technology in Funing Bay, China

Jinhua Huang [1], Baohang Wang [1,2], Xiaohe Cai [1,2,*], Bojie Yan [1], Guangrong Li [3], Wenhong Li [4], Chaoying Zhao [3], Liye Yang [5], Shouzhu Zheng [1] and Linjie Cui [1]

[1] School of Geography and Oceanography, Minjiang University, Fuzhou 350108, China; huangjinhua103@163.com (J.H.); wangbaohang@mju.edu.cn (B.W.); bnunercita@163.com (B.Y.); szzheng0304@mju.edu.cn (S.Z.); clj12211234@163.com (L.C.)
[2] Technology Innovation Center for Monitoring and Restoration Engineering of Ecological Fragile Zone in Southeast China, Ministry of Natural Resources, Fuzhou 350001, China
[3] School of Geological Engineering and Geomatics, Chang'an University, Xi'an 710054, China; 2020226022@chd.edu.cn (G.L.); cyzhao@chd.edu.cn (C.Z.)
[4] Xi'an Center of Geological Survey, China Geological Survey, Xi'an 710054, China; liwenhong01@mail.cgs.gov.cn
[5] College of Civil Engineering, Xiangtan University, Xiangtan 411105, China; yangliye@chd.edu.cn
* Correspondence: caixiaohe@mju.edu.cn

Abstract: Reclamation is an effective strategy for alleviating land scarcity in coastal areas, thereby providing additional arable land and opportunities for marine ranching. Monitoring the safety of artificial reclamation embankments is crucial for protecting these reclaimed areas. This study employed synthetic aperture radar interferometry (InSAR) using 224 Sentinel-1A data, spanning from 9 January 2016 to 8 April 2024, to investigate the deformation characteristics of the coastal reclamation embankment in Funing Bay, China. We optimized the phase-unwrapping network by employing ambiguity-detection and redundant-observation methods to facilitate the multitemporal InSAR phase-unwrapping process. The deformation results indicated that the maximum observed land subsidence rate exceeded 50 mm per year. The Funing Bay embankment exhibited a higher level of internal deformation than areas closer to the sea. Time-series analysis revealed a gradual deceleration in the deformation rate. Furthermore, a geotechnical model was utilized to predict future deformation trends. Understanding the spatial dynamics of deformation characteristics in the Funing Bay reclamation embankment will be beneficial for ensuring the safe operation of future coastal reclamation projects.

Keywords: InSAR; Funing Bay; reclamation embankments; future trends

check for updates

Citation: Huang, J.; Wang, B.; Cai, X.; Yan, B.; Li, G.; Li, W.; Zhao, C.; Yang, L.; Zheng, S.; Cui, L. Coastal Reclamation Embankment Deformation: Dynamic Monitoring and Future Trend Prediction Using Multi-Temporal InSAR Technology in Funing Bay, China. *Remote Sens.* **2024**, *16*, 4320. https://doi.org/10.3390/rs16224320

Academic Editor: Antonio Miguel Ruiz Armenteros

Received: 23 September 2024
Revised: 29 October 2024
Accepted: 17 November 2024
Published: 19 November 2024

1. Introduction

With rapid economic development and population growth in coastal areas, intensive infrastructure and industrial facilities are occupying a substantial amount of land, leading to significant challenges for land resources. Ocean reclamation has emerged as a strategy for various countries to provide substantial land resources in the short term [1]. This process of land reclamation has yielded significant social and economic benefits, including an increased food supply through the creation of new agricultural land, the attraction of more investment through new industrial development sites, and the provision of additional space for urban expansion [2]. However, factors such as additional loads from engineering construction, along with natural soil consolidation and compaction, can easily result in localized settlement, thereby jeopardizing the infrastructure in the vicinity. Most areas undergoing land reclamation and deformation will initially experience rapid deformation, followed by a phase of slower deformation, which can be characterized as a two-phase process [3]. Large-scale dynamic monitoring of deformation in land reclamation areas holds significant value and importance.

Numerous countries around the world engage in land reclamation [4]. According to incomplete statistics, from 1991 to 2015, China's cumulative land reclamation area from the sea exceeded 6418.9 km^2 [5,6]. Synthetic aperture radar interferometry (InSAR) technology can detect minor surface deformations and offers several advantages, including extensive spatial coverage, cost-effectiveness, high precision, and continuous monitoring. InSAR has been utilized to monitor various airports located on reclaimed land areas, such as Hong Kong Airport [7], Xiamen Airport [8,9], Dalian Airport [10], and Shanghai Airport [11]. Additionally, many coastal regions have undergone reclamation to support urban expansion. InSAR technology is employed to analyze deformation characteristics in various locations, including Mokpo, South Korea [12]; Urayasu, Japan [13]; Istanbul and Rize, Turkey [14]; Brest, France [15]; Macao, China [16]; Penny's Bay Reclamation in Hong Kong, China [17]; Shenzhen, China, [18]; Tianjin, China [19]; Singapore [20]; and Shanghai, China [21,22]. The dynamic monitoring of the stability of reclamation areas holds significant value [23,24].

Several multitemporal InSAR techniques have been proposed, including persistent scatterer InSAR (PS-InSAR) [25], point-target analysis (IPTA) [26], the Stanford method for persistent scatterers (StaMPSs) [27], and permanent scatterer pairs (PSPs) [28]. Additionally, small baseline subset (SBAS)-InSAR [29] and spatiotemporal-filtering-based distributed scatterer InSAR (DS-InSAR) techniques analyze ground displacements of distributed scatterer (DS) targets, including SqueeSAR [30], phase link (PL) [31], and other advanced multitemporal InSAR techniques [32–37]. These advanced multitemporal InSAR techniques have been comprehensively reviewed in references [38–41]. Continuous SAR observation data, such as those from Sentinel-1A, which has a revisit interval of 12 days, are expected to increase exponentially. Additionally, onboard commercial satellites, including Radarsat-2, ALOS-2, TerraSAR-X/TanDEM-X/PAZ, and NASA-ISRO SAR (NISAR), will further enrich the SAR data pool. The emerging SAR data have the potential to support real-time online services, early warning systems, and various engineering applications [42]. InSAR technology is an indispensable tool for Earth observation and has been utilized to assess various infrastructures [43], including railways [44,45], bridges [46,47] and reservoir dams [48,49]. Several InSAR dynamic deformation monitoring technologies have been developed to obtain deformation parameters in near real-time [50–54].

In addition, predicting ground subsidence can help identify abnormal geological phenomena in advance, which is crucial for preventing subsidence-related disasters and implementing timely preventive measures. This is particularly important in reclaimed areas, where the underlying soil exhibits high compressibility and requires an extended period to compact and solidify. The methods for predicting settlement using InSAR deformation time series in land reclamation include theoretical estimations based on soil consolidation theory [9,55], curve-fitting mathematical models [56–58], and deep learning techniques [59,60].

Unlike reservoir dams, this research employed multitemporal InSAR technology to dynamically assess the spatiotemporal deformation characteristics of the coastal reclamation embankment located in Funing Bay, China, which resembles a bridge spanning the sea area. The reclamation embankment undergoes both settlement due to soil consolidation and erosion caused by water on either side of the structure. This study incorporated network optimization techniques to facilitate high-precision phase unwrapping, thereby enhancing the reliability of dynamic deformation monitoring. Subsequently, sequential least squares were utilized to continuously update the deformation parameters of the reclamation embankment. Ultimately, we analyzed the deformation characteristics of the reclamation embankment and predicted its future trends.

2. Study Area SAR Dataset

The reclamation project in Funing Bay is crucial for facilitating the rapid construction and implementation of modern agricultural practices, including the establishment of sea grain warehouses, in Fujian Province, China. Additionally, it supports the expansion of urban space while safeguarding Xiapu, China, from the devastating effects of typhoons. The Funing Bay reclamation area is situated within Ningde City, China, and was developed between 2007 and 2012. The total area of the reclaimed land spans 34,100 acres. The primary objective of the project was the construction of reclamation embankment. The reclamation embankment is approximately 5434 m in length and 85 m in width, with an elevation of about 9.6 m [61].

Figure 1 presents optical images, a synthetic aperture radar (SAR) intensity image, and on-site photographs of the reclamation embankment. Panels (A), (B), and (C) were captured in 2005, 2010, and 2020, respectively, using Google Earth. Panel (D) displays the Sentinel-1A SAR intensity image within a coordinate system defined by range and azimuth. The heading angle of the Sentinel-1A SAR satellite was -12.5 degrees. The P point in Panel (C) illustrates the soil composition and its compression characteristics.

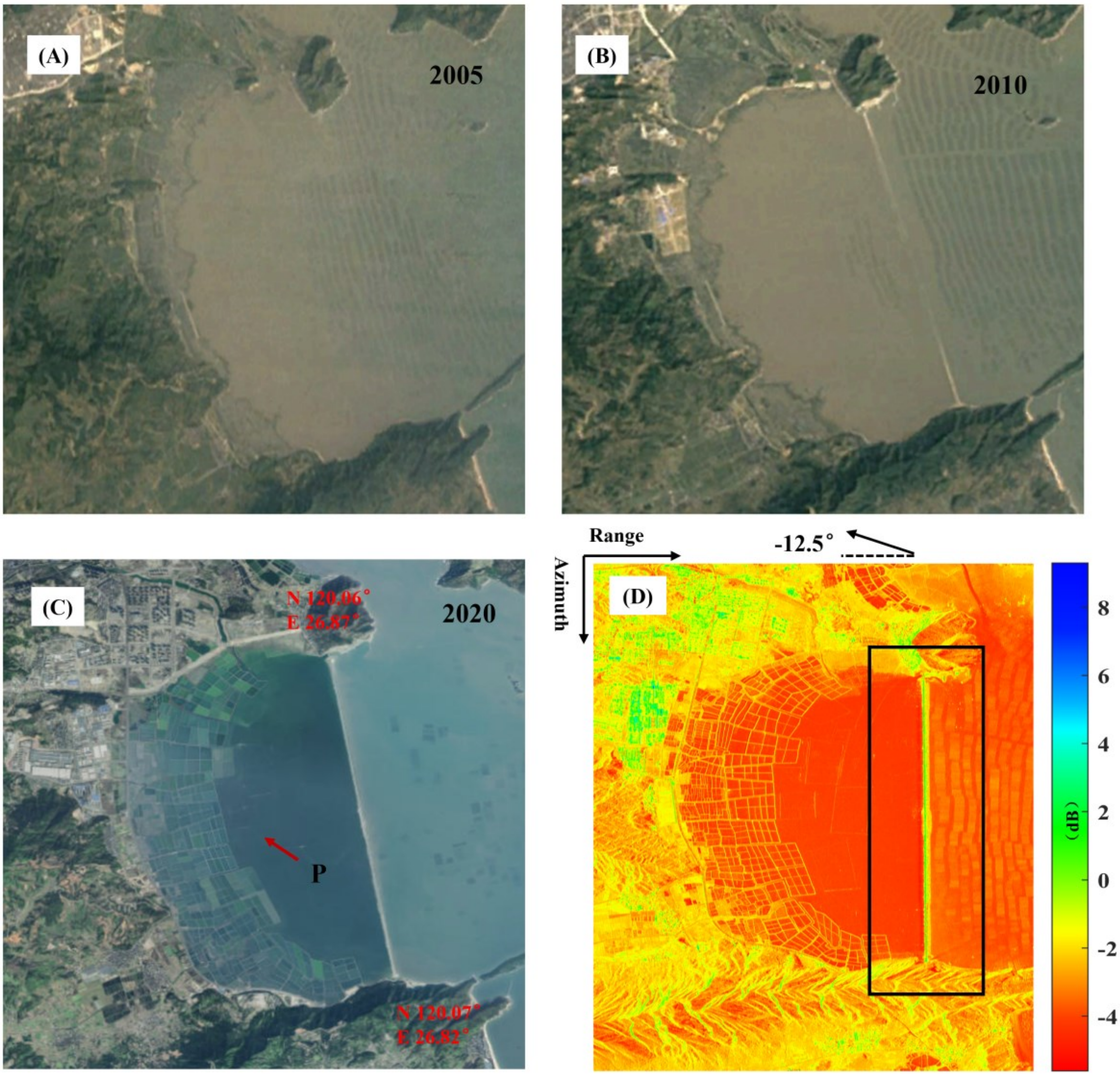

Figure 1. The optical images from Google Earth, captured in 2005 (**A**), 2010 (**B**), and 2020 (**C**), are presented here. Panel (**D**) displays the average intensity image from Sentinel-1A SAR, with the rectangular area highlighting the reclamation embankment of Funing Bay, China.

We collected 224 Sentinel-1A SAR data from 6 January 2016 to 8 April 2024, to monitor the deformation characteristics of the reclamation embankment in Funing Bay. Additionally, we generated 860 small baseline (SB) interferograms at full resolution, as illustrated in Figure 2. The red small circles represent the 224 SAR data, and the blue line indicates interferograms.

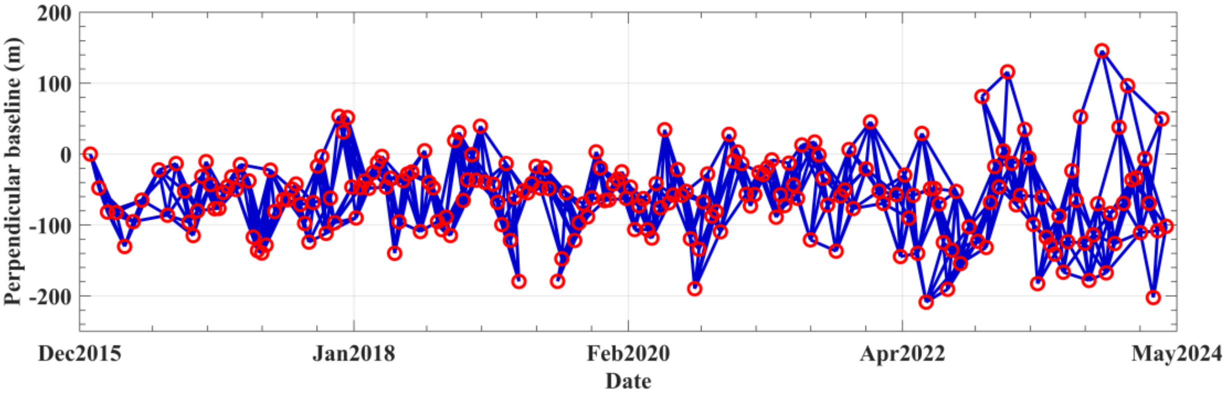

Figure 2. Spatiotemporal baseline of SB interferograms.

3. Methodology

Figure 3 illustrates the workflow for dynamic monitoring and future trend prediction of coastal reclamation embankments using InSAR technology. Initially, we utilized external Shuttle Radar Topography Mission (SRTM) digital elevation model data, precise orbital data, and Sentinel-1A data to generate SB interferograms [29]. Next, we applied the Goldstein filtering method to each interferogram [62,63]. These operations were performed using the Gamma SAR processor and interferometry 2015 software. Subsequently, we utilized MATLAB R2022 software to process the InSAR phase unwrapping and extract deformation parameters. A temporal coherence threshold was implemented to select high-quality pixels [64]. Following this, we optimized the phase-unwrapping network using K-nearest neighbors (KNNs), ambiguity-detection methods, and the number of redundant observations. After phase unwrapping with the Edgelist algorithm and error phase estimation, we dynamically updated the InSAR deformation parameters using sequential least squares. Finally, we predicted deformation using a geotechnical model and conducted a comprehensive analysis.

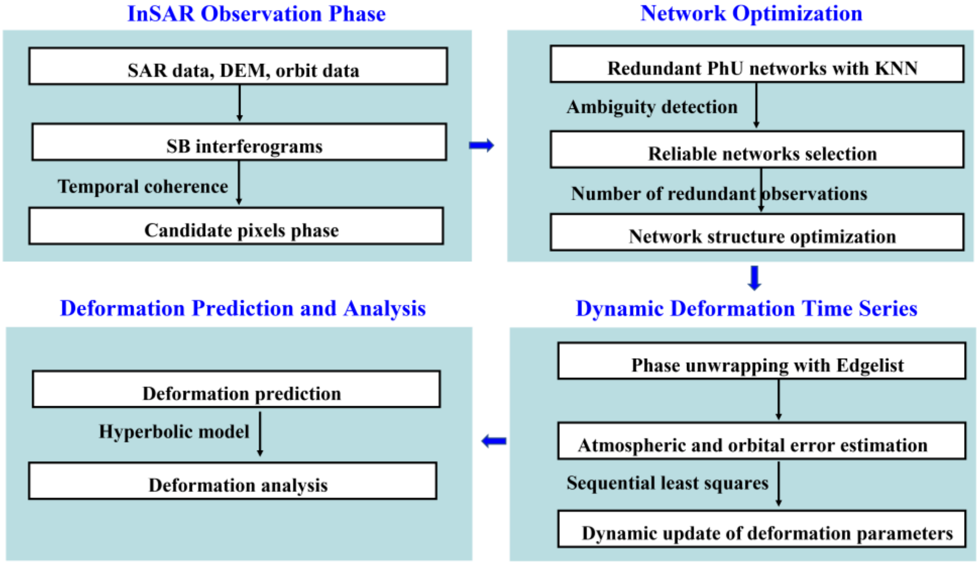

Figure 3. Workflow for InSAR deformation dynamic monitoring and future trend prediction of coastal reclamation embankments.

3.1. Network-Optimization-Assisted InSAR Phase Unwrapping

In InSAR phase unwrapping, the minimum cost flow (MCF) method utilizes the Delaunay network; however, this network is not optimal. Network-optimization techniques can identify the optimal path to enhance the reliability of phase unwrapping [65–67]. First, we implemented the K-nearest neighbors (KNNs) algorithm to generate redundant candidate spatial phase-unwrapping networks, replacing the traditional Delaunay triangulation networks. Subsequently, we employed an ambiguity-detection method [68] to establish a reliable network, thereby improving the performance of the L1 norm spatial phase unwrapping, as demonstrated in Equation (1):

$$\begin{aligned}
&\mathbf{A}_{M\times N}\Delta\boldsymbol{\theta}^{p,q}_{N\times 1}=\Delta\boldsymbol{\varphi}^{p,q}_{M\times 1}\\
&\Delta\boldsymbol{\varphi}^{p,q}_{M\times 1}-\mathbf{A}^{p,q}_{M\times N}\left(\mathbf{A}^{T}_{M\times N}\mathbf{A}_{M\times N}\right)^{-1}\mathbf{A}^{T}_{M\times N}\Delta\boldsymbol{\varphi}^{p,q}_{M\times 1}=\Delta^{p,q}
\end{aligned} \tag{1}$$

where the $\mathbf{A}_{M\times N}$, $\Delta\boldsymbol{\varphi}^{p,q}_{M\times 1}$, and $\Delta\boldsymbol{\theta}^{p,q}_{N\times 1}$ are the design matrix, double-difference phase in M interferograms, and N wrapped phase time-series between pixels p and q, respectively. We utilized the least-squares phase residual time series in arcs $\Delta^{p,q}$ with a predetermined threshold $\max|\Delta^{p,q}| < T_{residual}$ to select reliable arcs.

Next, we employed a strategy involving redundant observations [67] to optimize phase unwrapping networks and control the reliability of the network structure with $Pixel_i^{NRO} < T_{NRO}$, where the $Pixel_i^{NRO}$ and T_{NRO} are the number of redundant observations for each pixel and a predetermined threshold, respectively. Finally, we applied the Edgelist algorithm [65–67,69] to execute spatial phase unwrapping, as demonstrated in Equation (2):

$$\begin{aligned}
&min\left(f^{+}_{1\times D}\boldsymbol{K}^{+}_{D\times 1}-f^{-}_{1\times D}\boldsymbol{K}^{-}_{D\times 1}\right)\\
&s.t.\begin{bmatrix}\mathbf{C}_{D\times P} & -\mathbf{C}_{D\times P} & \mathbf{I}_{D\times D} & \mathbf{I}_{D\times D}\end{bmatrix}\begin{bmatrix}\boldsymbol{L}^{+}_{P\times 1}\\ \boldsymbol{L}^{-}_{P\times 1}\\ \boldsymbol{K}^{+}_{D\times 1}\\ \boldsymbol{K}^{-}_{D\times 1}\end{bmatrix}=\Delta\boldsymbol{\varphi}^{m}_{D\times 1}\\
&with\quad L^{+},L^{-},K^{+},K^{-}\ \in\mathbb{N}^{0}
\end{aligned} \tag{2}$$

where $\mathbf{C}$ coefficient matrix with elements of -1, 0, and 1 corresponding to optimized network arcs. The P and D are the number of the selected pixels and optimized arcs, respectively. I is the unit matrix. $\boldsymbol{K}^{+}_{D\times 1}$ and $\boldsymbol{K}^{-}_{D\times 1}$ show the ambiguities of optimized arcs. $\boldsymbol{L}^{+}_{P\times 1}$ and $\boldsymbol{L}^{-}_{P\times 1}$ show pixel ambiguities to obtain unwrapped interferogram by $\boldsymbol{\theta}^{m}_{P\times 1}=\boldsymbol{L}^{+}_{P\times 1}-\boldsymbol{L}^{-}_{P\times 1}$.

Next, we used the temporal coherence (γ_{LS}) of the residual phase to assess the reliability of phase unwrapping [70], as shown in Equation (3):

$$\begin{aligned}
&\gamma_{LS}=\frac{1}{M}\left|\sum_{i=1}^{M}\exp\left\{j\left(\boldsymbol{\theta}_{M\times 1}-\mathbf{A}_{M\times N}\overline{\boldsymbol{\theta}}_{N\times 1}\right)\right\}\right|\\
&\overline{\boldsymbol{\theta}}_{N\times 1}=\left(\mathbf{A}^{\mathrm{T}}_{M\times N}\mathbf{A}_{M\times N}\right)^{-1}\mathbf{A}^{\mathrm{T}}_{M\times N}\boldsymbol{\theta}_{M\times 1}
\end{aligned} \tag{3}$$

where $\mathbf{A}_{M\times N}$, $\boldsymbol{\theta}_{M\times 1}$, and $\overline{\boldsymbol{\theta}}_{N\times 1}$ are the design matrix, unwrapped phases, and the estimated unwrapped-phase time-series, respectively.

3.2. Dynamic Estimation of InSAR Deformation Time-Series

After obtaining reliable unwrapped-phase and correcting-phase errors, we employed least squares to estimate the deformation time series $\boldsymbol{X}_1$ and its cofactor matrix $\boldsymbol{Q}_{X_1}$. Following the acquisition of new SAR data and their corresponding unwrapped interferogram $\boldsymbol{L}_2$, we utilized sequential least squares to update the deformation time series using Equation (4) [50]:

$$\begin{aligned}\begin{bmatrix} \boldsymbol{X}_2 \\ Y \end{bmatrix} &= \begin{bmatrix} \boldsymbol{X}_1 + \mathbf{J}_x(\boldsymbol{L}_2 - \mathbf{A}_2\boldsymbol{X}_1 - \mathbf{B}Y) \\ (\mathbf{B}^{\mathrm{T}}\boldsymbol{Q}_J{}^{-1}\mathbf{B})^{-1}\mathbf{B}^{\mathrm{T}}\boldsymbol{Q}_J{}^{-1}(\boldsymbol{L}_2 - \mathbf{A}_2\boldsymbol{X}_1) \end{bmatrix} \\ \boldsymbol{Q}_{\left[\begin{smallmatrix} \boldsymbol{X}_2 \\ Y \end{smallmatrix}\right]} &= \begin{bmatrix} \boldsymbol{Q}_{X_1} - \mathbf{J}_x\mathbf{A}_2\boldsymbol{Q}_{X_1} + \mathbf{J}_x\mathbf{B}\boldsymbol{Q}_Y\mathbf{B}^{\mathrm{T}}\mathbf{J}_x^{\mathrm{T}} & -\mathbf{J}_x\mathbf{B}\boldsymbol{Q}_Y \\ (-\mathbf{J}_x\mathbf{B}\boldsymbol{Q}_Y)^{\mathrm{T}} & (\mathbf{B}^{\mathrm{T}}\boldsymbol{Q}_J{}^{-1}\mathbf{B})^{-1} \end{bmatrix}\end{aligned} \tag{4}$$

in which $\mathbf{J}_x = \boldsymbol{Q}_{X_1}\mathbf{A}_2{}^{\mathrm{T}}\boldsymbol{Q}_J{}^{-1}$ and $\boldsymbol{Q}_J = \mathbf{P}_2^{-1} + \mathbf{A}_2\boldsymbol{Q}_{X_1}\mathbf{A}_2{}^{\mathrm{T}}$ are the gain matrix and its updated cofactor matrixes, respectively. The $\mathbf{A}_2$ and $\boldsymbol{B}$ correspond to archived and newly designed matrices of unwrapped SB interferograms [50]. $\boldsymbol{X}_2$ and Y are updated InSAR archived deformation time series and the latest cumulative deformation time series, respectively.

3.3. Reclamation Embankment Deformation Prediction with Geotechnical Model

In reclamation areas, soil consolidation deformation processes are categorized into empirical models and geotechnical models. The hyperbolic model can accurately predict deformation processes that exhibit deceleration trends, effectively capturing nonlinear changes. This method can be rapidly applied to determine the parameters of the curve function, making it particularly well-suited for forecasting ground subsidence in reclaimed land [56–58,71], as demonstrated in Equation (5):

$$W_t = W_0 + \frac{t - t_0}{a + b(t - t_0)} \tag{5}$$

where $W(t)$ is the subsidence deformation at time t with respect to the reference time t_0 and deformation W_0. The a and b are the shape parameters of the curve model, respectively.

A geotechnical model was utilized to predict the future evolution of ground subsidence at Xiamen Airport in China [9]. Unlike mathematical curve fitting, this article employed a geological model with physical significance to predict the future deformation trends of the Funing Bay reclamation embankment [9,72], as demonstrated in Equation (6):

$$W_t = S\frac{t^{\lambda}}{K^{\lambda} + t^{\lambda}} \tag{6}$$

where $W(t)$ is the subsidence deformation at time t with respect to the reference time t_0. The S is the possible maximum subsidence. k and λ are the shape parameters of the curve model. This empirical model is quite rigorous in selecting initial values, as the inappropriate selection of initial parameter values can significantly affect the performance of the deformation model [9,72]. The parameters of the curve function in this model are exponential and difficult to converge, requiring numerous iterations to determine suitable initial values.

4. Results

4.1. Deformation Results

First, we utilized the temporal coherence of the wrapped phase to select candidate pixels [64]. Next, we generated redundant phase-unwrapping networks using K-nearest neighbors (KNNs) with a threshold of 1000 from these candidate pixels and selected reliable networks through ambiguity-detection methods. In order to balance the network structure and improve the efficiency of phase unwrapping, we optimized the structure of these reliable networks using a strategy based on redundant observations. Subsequently, we applied L1 norm phase unwrapping with the Edgelist algorithm, utilizing the optimized networks for phase unwrapping. The deformation rate was estimated using all unwrapped SB interferograms, as illustrated in Figure 4, where points P1–P5 will demonstrate the deformation time series. The deformation characteristics of the reclamation embankment in Funing Bay are quite pronounced.

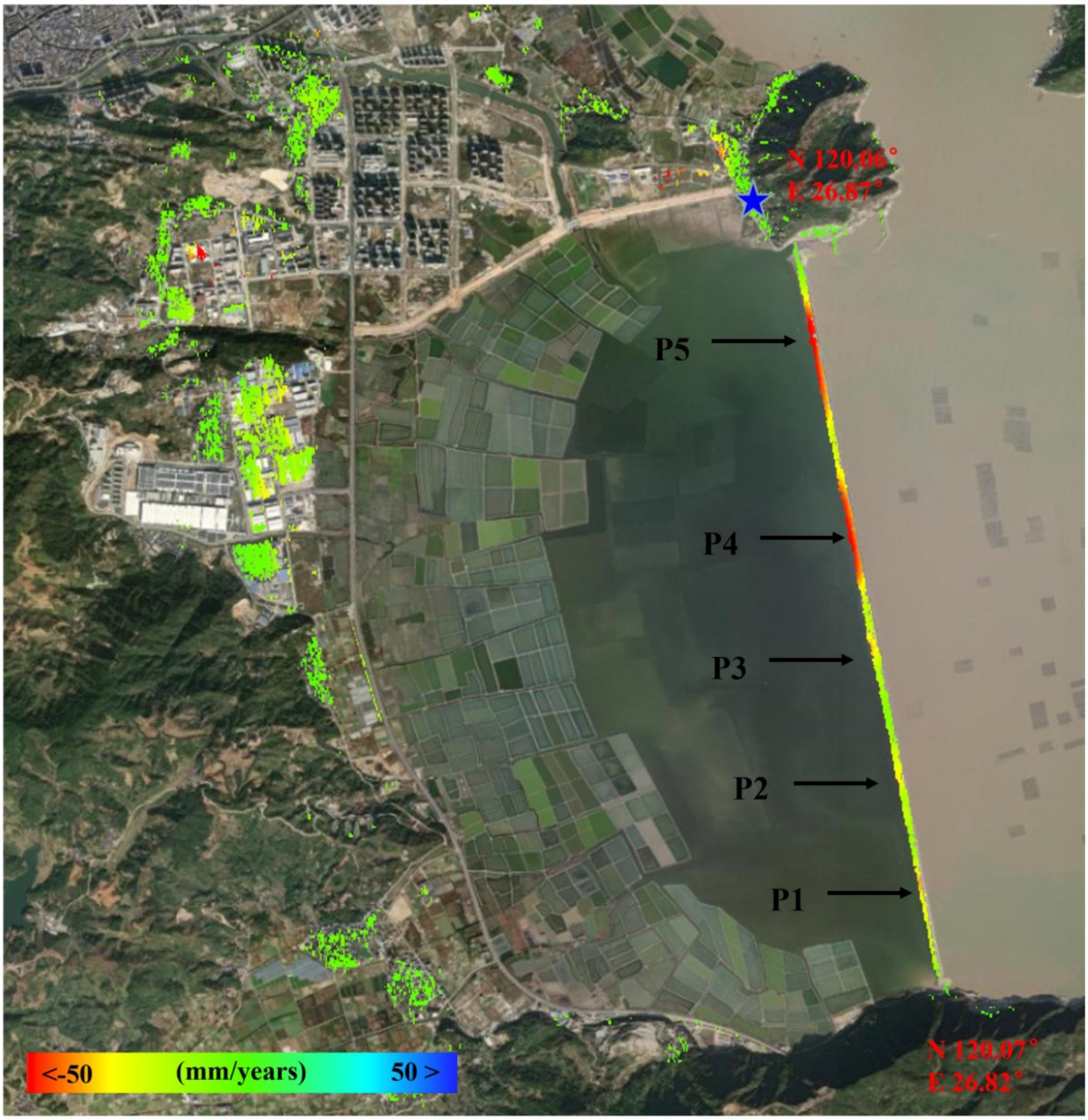

Figure 4. The deformation rate, where the blue pentagram serves as the reference point for phase unwrapping.

The wrapped interferograms provide a direct visualization of the deformation characteristics of the Funing Bay reclamation embankment. We utilized the most recent SAR data from 8 April 2024, as a reference image to generate single-master interferograms. Figure 5 presents eight interferograms with a time interval of 120 days, corresponding to ten SAR data sets. Panels (A–H) represent time periods of 984, 828, 672, 552, 420, 300, 180, and 60 days, respectively. They clearly demonstrate the deformation characteristics of the Funing Bay embankment in the wrapped phase.

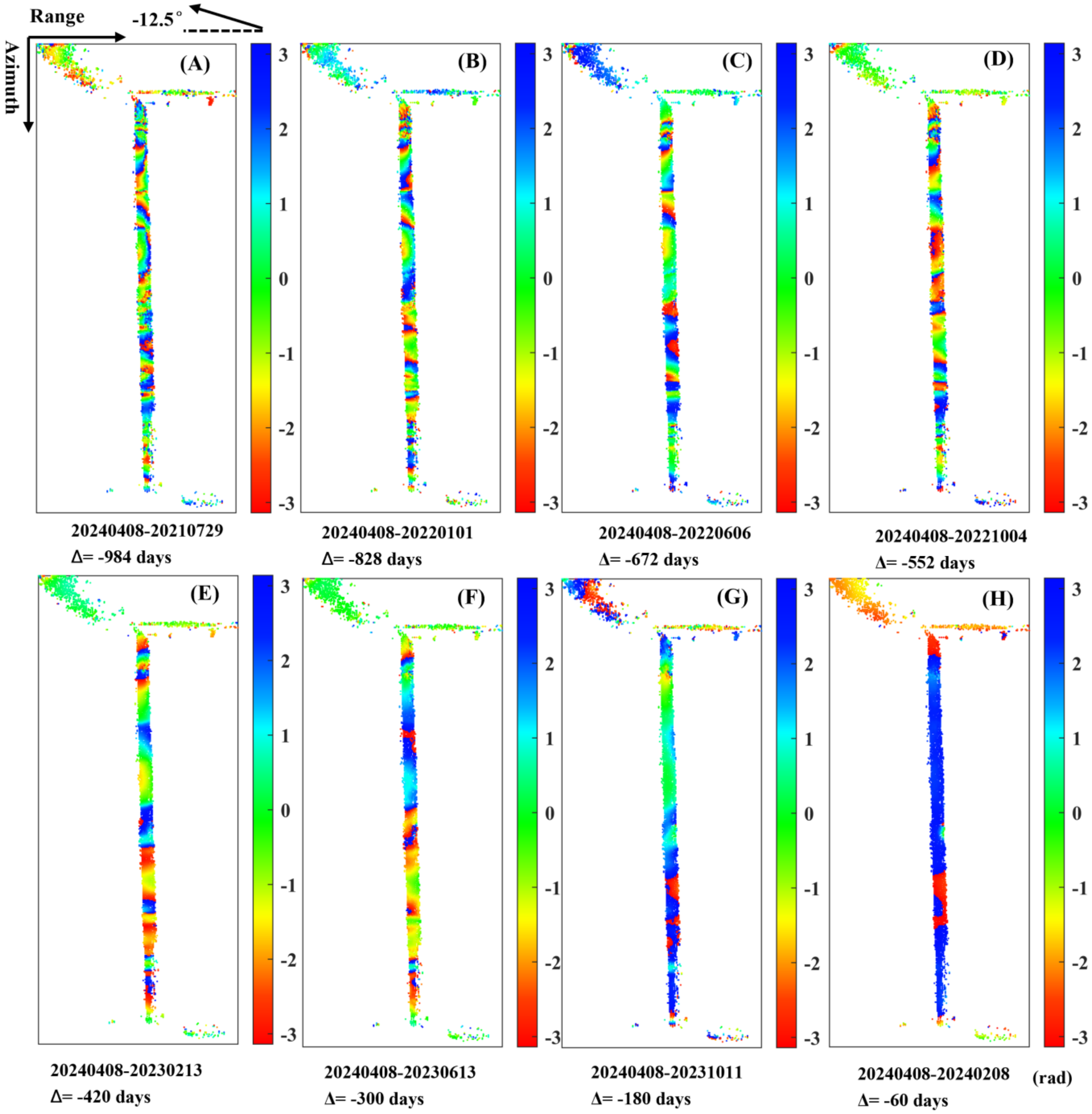

Figure 5. Panels (**A**–**H**) represent eight interferograms corresponding to time periods of 984, 828, 672, 552, 420, 300, 180, and 60 days, respectively.

In addition, we plotted the deformation time series at the locations indicated by arrows P1–P5 in Figure 4, as illustrated in Figure 6. Figure 6A illustrates the reclamation embankment, with particular emphasis on the black rectangular area. The deformation time series for points P1 to P5 is depicted in Figure 6B–F. The blue dots represent the deformation time series, while the red lines indicate the fitted linear deformation rates. Overall, the characteristics of the deformation rates appeared to be slow, which was generally consistent with the deformation patterns observed in land reclamation areas. Regions with high deformation rates, such as P4 and P5, had experienced a total settlement of 400 mm from 9 January 2016 to 8 April 2024.

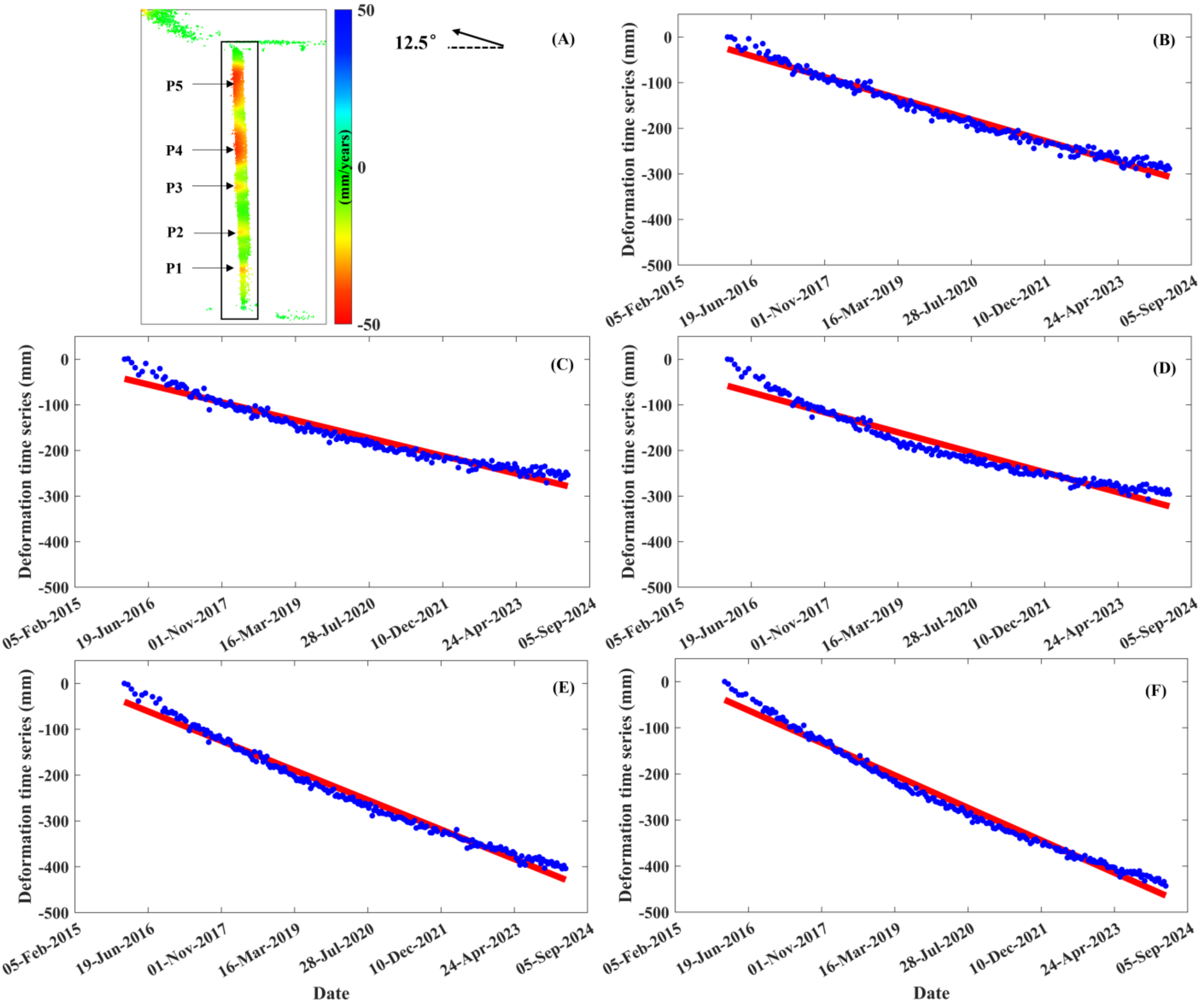

Figure 6. (**A**) is reclamation embankment, where P1–P5 correspond to the deformation time series (**B**–**F**), respectively.

To illustrate the deformation characteristics of the Funing Bay reclamation embankment, we present a locally enlarged deformation rate, as shown in Figure 7A. Arrow P1 indicates the longitudinal deformation rate profile of the reclamation embankment, as depicted in Figure 7B. The entire reclamation embankment had experienced subsidence; however, the spatial distribution of this subsidence was uneven. Panel (C) displays the acceleration of the deformation time series recorded on 8 April 2024. The results indicate that the deformation acceleration at positions P2, P5, and P6 was relatively high, while positions P3 and P4 exhibit lower deformation rates. Positions P2 to P6 represent the transverse deformation rate profile, illustrated in Figure 8. It is evident that the deformation rate of the reclamation dam on the left side was greater than that on the outer side.

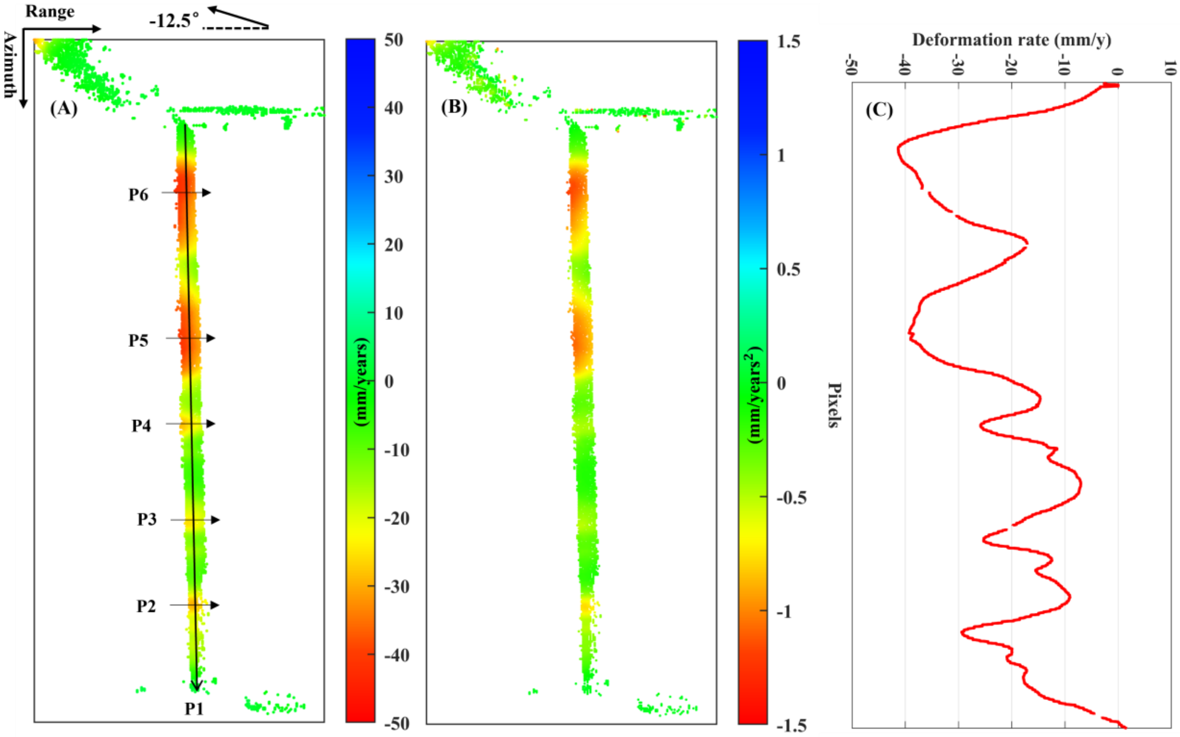

Figure 7. The deformation rate of the reclaimed embankment (**A**), the acceleration of the deformation rate at the most recent time (**B**), and the deformation rate profile of the reclaimed embankment (**C**) are illustrated as P1 in (**A**).

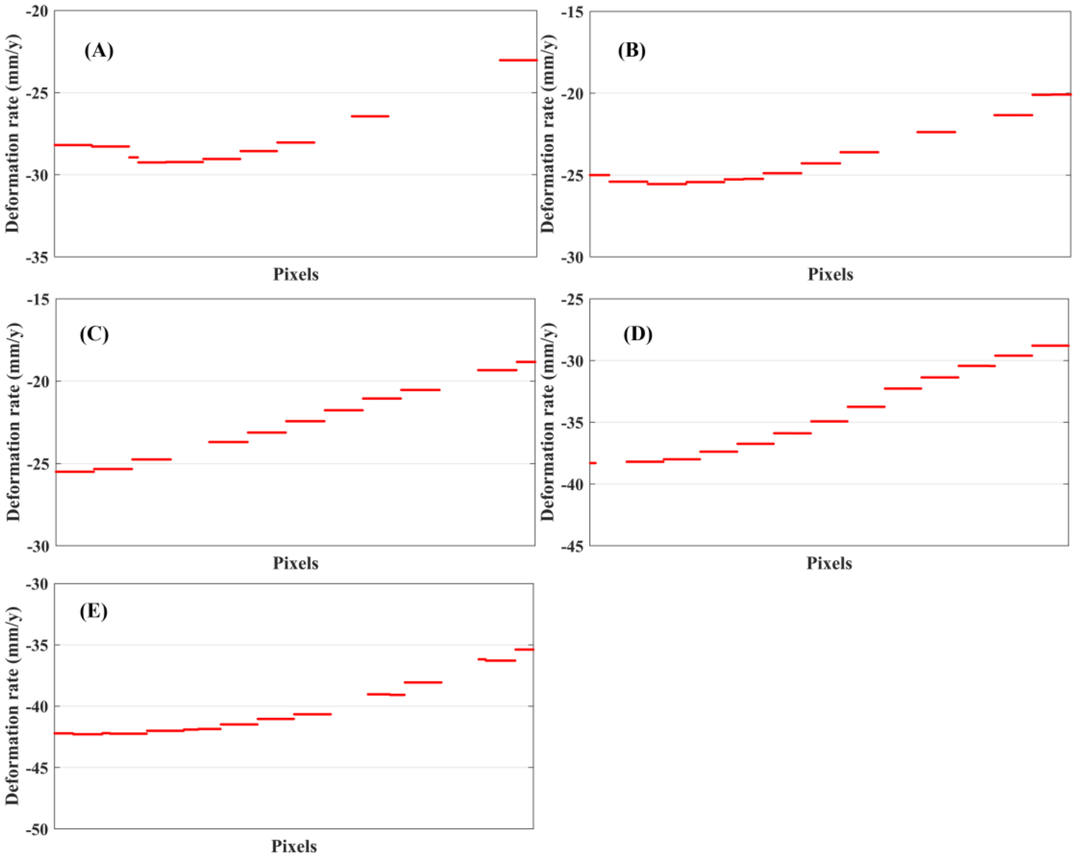

Figure 8. The cross-section of the deformation rate, where (**A**–**E**) correspond to P2–P6 in Figure 7.

4.2. InSAR Deformation Reliability Analysis

To assess the reliability of InSAR deformation parameters, we demonstrated the temporal coherence of phase unwrapping, as illustrated in Figure 9A. The temporal coherence consistently exceeded 0.7, particularly on the embankment, thereby confirming the reliability of the phase-unwrapping process. Additionally, to further assess the reliability of the deformation time series, we calculated the standard deviation of the deformation time series for each pixel after correcting for DEM errors, as shown in Figure 9B. The standard deviation of the deformation time series was primarily concentrated within 3 mm on the embankment.

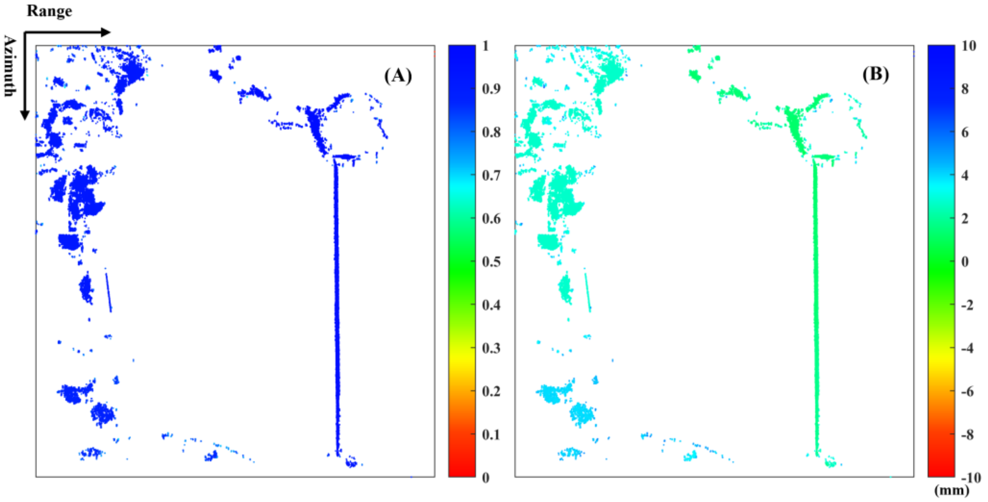

Figure 9. The temporal coherence of the unwrapped phase is indicated as (**A**), while the standard deviation of the deformation time series is represented as (**B**).

4.3. Deformation Model

The temporal and spatial characteristics of the deformation of the Funing Bay reclamation dam have been discussed above. We analyzed the standard deviation of residual deformation after modeling for both the hyperbolic model and the geological model, as illustrated in Figure 10. The average standard deviation of the residual deformation after fitting the hyperbolic model was 5.1 mm, while the geological model achieved a lower average standard deviation of 3.5 mm. Subsequently, we utilized the geological model to predict the future deformation trend of the Funing Bay dam, as shown in Figure 11.

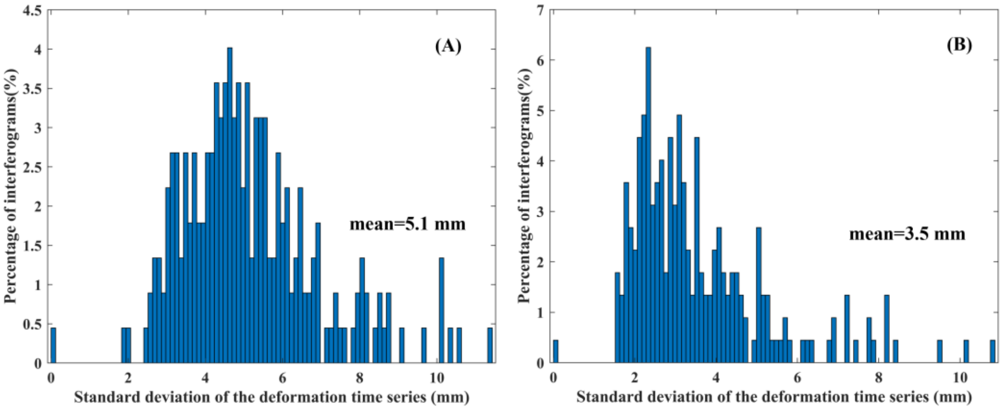

Figure 10. A statistical histogram illustrating the standard deviation of residual deformation after modeling, where (**A**) represents the hyperbolic model and (**B**) denotes the geological model.

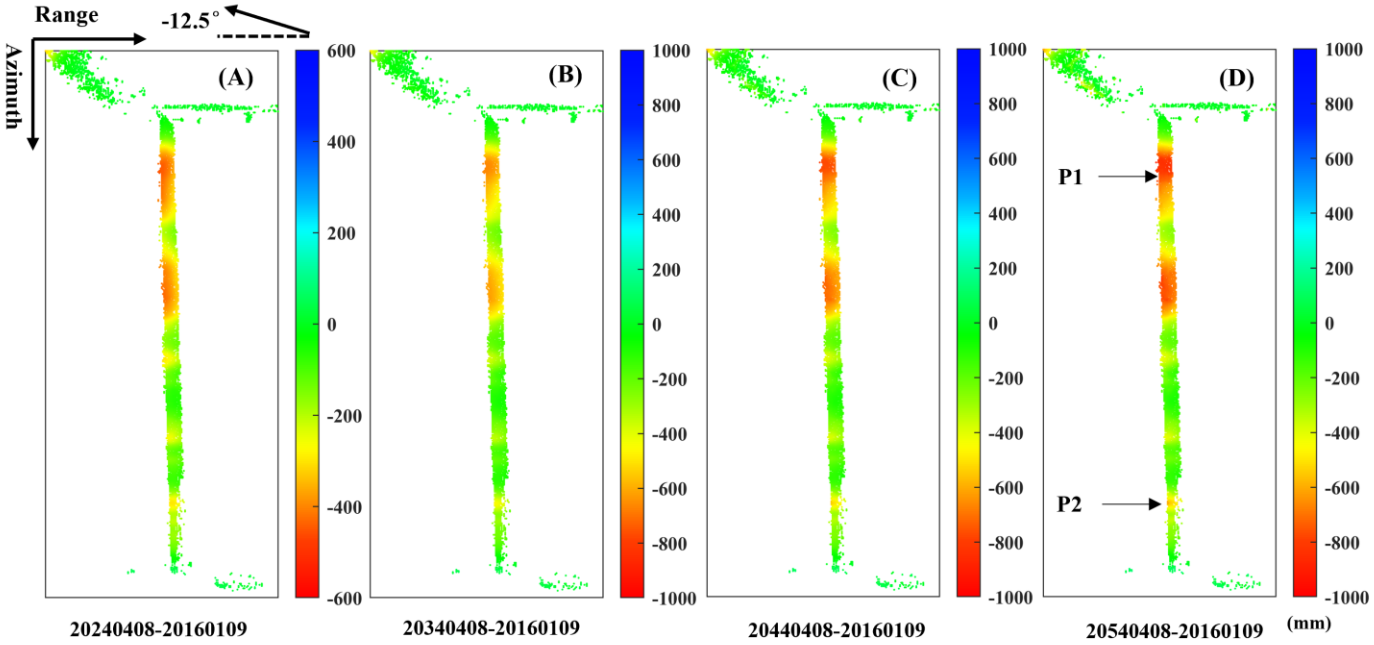

Figure 11. Estimated cumulative deformations using 224 SAR data (**A**) and predicted cumulative deformations for the next 10 (**B**), 20 (**C**), and 30 (**D**) years. Points A and B will show deformation time series in Figure 12.

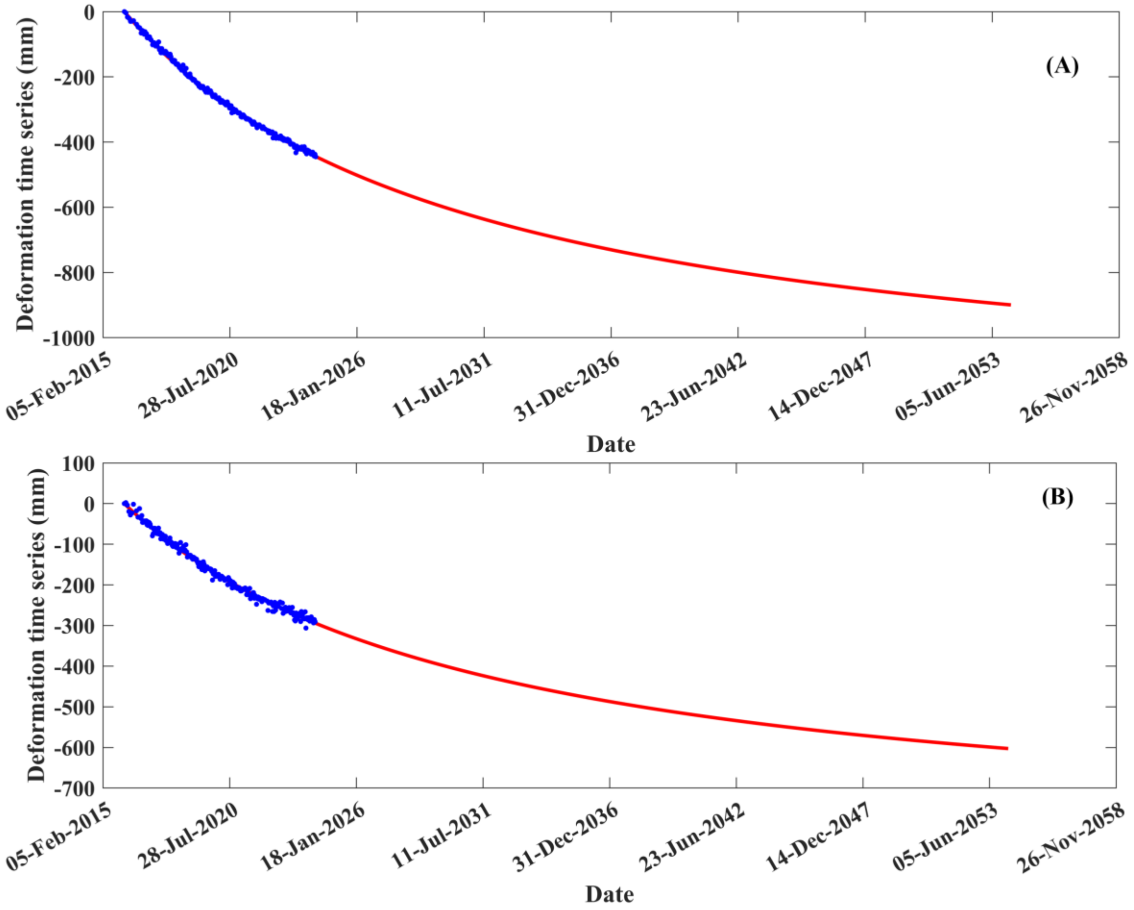

Figure 12. Predicted cumulative deformation time series, where (**A**,**B**) correspond to points P1 and P2 in Figure 9.

Figure 11A represents the cumulative deformation derived from 224 SAR data, while Figure 11B–D depict the predicted cumulative deformations for the next 10, 20, and 30 years, respectively, corresponding to the dates of 8 April 2034, 8 April 2044, and 8 April 2054. Figure 12A,B illustrate the predicted cumulative deformation time series for P1 and P2 in Figure 11D, respectively. The blue dots represent the 224 SAR data, and the red line indicates the fitted curve. Over the next 30 years, the reclamation embankment of Funing Bay is expected to undergo significant deformation, with cumulative deformation reaching 1000 mm.

5. Discussion

During the construction of the Funing Bay reclamation embankment, blasting and silt-squeezing methods were utilized. The construction conditions of the Funing Bay reclamation embankment were suboptimal, and there are no islands or reefs in the middle, as shown in Figure 1. According to 42 years of continuous data collected from the Sansha Ocean Observation Station, the annual average highest tide level was 3.74 m, while the lowest tide level was −3.48 m. The highest recorded tide level was 4.4 m, resulting in a maximum tidal range of 8.04 m [61]. Additionally, the embankment is situated in proximity to the open sea, rendering it vulnerable to the impact of surging waves.

Figure 13 presents images from the on-site investigation of the reclamation embankment. In Figure 13A, the embankment is depicted, with the reclaimed area on the left and the ocean on the right. The water level of the seawater is higher than that of the reclaimed area. The red arrow in Figure 13B illustrates the lateral inclination of the embankment, while the red arrow in Figure 13C indicates that the embankment has already settled.

Figure 13. On-site photographs of the reclamation embankment (**A**). The red arrows in (**B**,**C**) indicate the occurrence of tilting and settlement of the embankment, respectively.

The foundation of the Funing Bay reclamation embankment consists of a heterogeneous mixture that includes silt, mucky soil, silty clay, and gravel. This foundation is composed of five layers, arranged from top to bottom [61]. The geological conditions of the seawall foundation reveal that the bearing layer consists of a deep soft foundation made up of silt and silty soil layers, with a silt thickness of approximately 20 m. Figure 14 presents the results of geotechnical exploration at point P, as illustrated in Figure 1C. The first column displays two layers of soil: silt and silty clay. The second column indicates the thickness of each soil layer, while the third column represents the depth at which geotechnical exploration testing was conducted. The fourth and fifth columns provide shear strength measurements for undisturbed and remolded soil, respectively. The sixth column denotes sensitivity, defined as the ratio of shear strength between undisturbed and remolded soil. The seventh column lists the depth values from the geotechnical exploration, and the eighth column illustrates the linear relationship between the shear strength of undisturbed silt soil and burial depth. Notably, as depth increases, the shear strength of silt also increases. The deformation characteristics of the completed reclamation embankment may be attributed to the compaction of cement and concrete that has accumulated on the soil layer.

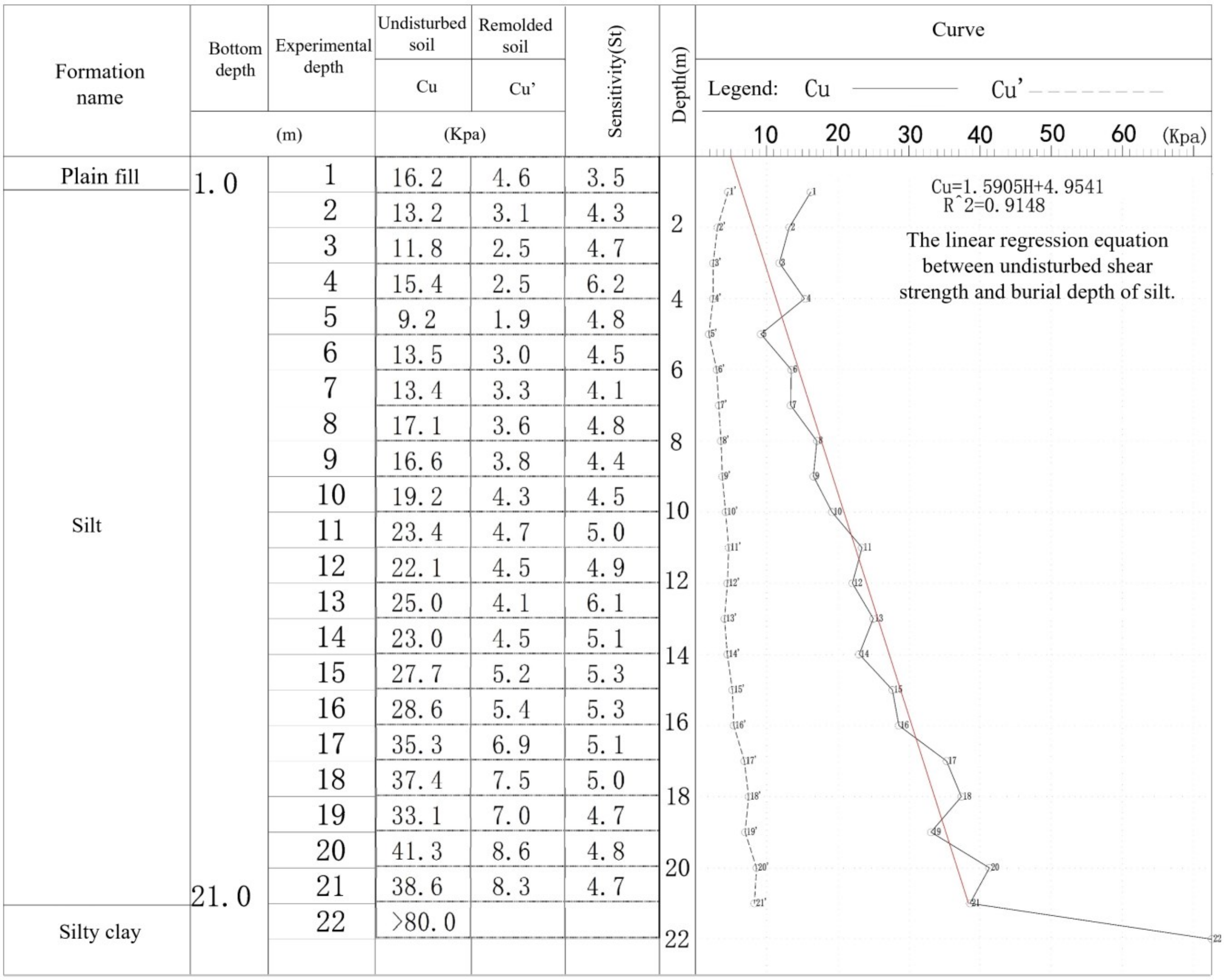

Formation name	Bottom depth (m)	Experimental depth (m)	Undisturbed soil Cu (Kpa)	Remolded soil Cu' (Kpa)	Sensitivity(St)
Plain fill	1. 0	1	16. 2	4. 6	3. 5
Silt		2	13. 2	3. 1	4. 3
		3	11. 8	2. 5	4. 7
		4	15. 4	2. 5	6. 2
		5	9. 2	1. 9	4. 8
		6	13. 5	3. 0	4. 5
		7	13. 4	3. 3	4. 1
		8	17. 1	3. 6	4. 8
		9	16. 6	3. 8	4. 4
		10	19. 2	4. 3	4. 5
		11	23. 4	4. 7	5. 0
		12	22. 1	4. 5	4. 9
		13	25. 0	4. 1	6. 1
		14	23. 0	4. 5	5. 1
		15	27. 7	5. 2	5. 3
		16	28. 6	5. 4	5. 3
		17	35. 3	6. 9	5. 1
		18	37. 4	7. 5	5. 0
		19	33. 1	7. 0	4. 7
		20	41. 3	8. 6	4. 8
	21. 0	21	38. 6	8. 3	4. 7
Silty clay		22	>80. 0		

Figure 14. Geotechnical exploration at point P, as illustrated in Figure 1C.

6. Conclusions

Land reclamation is a prevalent practice in coastal regions. This study employed multitemporal InSAR technology to dynamically monitor the embankment reclamation of

Funing Bay, China. A reliable phase-unwrapping method was utilized to obtain precise deformation results. The analysis of deformation rates, profiles, and on-site investigation results indicated that the embankment reclamation exhibited significant deformation characteristics. The findings of this research suggest that the deformation of the embankment reclamation will persist over the next 30 years, with deformation levels in certain areas likely to exceed 1000 mm. Furthermore, potential deformation levels and trends in the embankment reclamation over the next three decades were predicted using a geotechnical model. These deformation characteristics present challenges to the safe operation of the dam. The dynamic monitoring of reclaimed embankments using InSAR technology is critically important, as it contributes to the effective management and safety of such structures.

Author Contributions: B.W. and G.L. performed the experiments and produced the results. B.W., J.H. and X.C. drafted the manuscript. B.Y., W.L., C.Z. and L.Y. finalized the manuscript. S.Z. and L.C. conducted on-site investigations. All authors have read and agreed to the published version of the manuscript.

Funding: This research was funded by the Natural Science Foundation of China under grants (Nos. 42304034 and 42474029), the Fujian Province Natural Resources Science and Technology Innovation Project (No. KY-030000-04-2024-034), the Fujian Provincial Natural Science Foundation of China (No. 2023J05257), and the Initial Scientific Research Fund of Talents in Minjiang University (No. MJY23002).

Data Availability Statement: The data presented in this study are available on request from the corresponding author.

Acknowledgments: Thanks to the European Space Agency for providing the Sentinel-1A data. The authors would like to thank the Technology Innovation Center for Monitoring and Restoration Engineering of Ecological Fragile Zone in Southeast China, Ministry of Natural Resources for providing the geotechnical exploration data.

Conflicts of Interest: The remaining authors declare that the research was conducted in the absence of any commercial or financial relationships that could be construed as a potential conflict of interest.

References

1. Martín-Antón, M.; Negro, V.; del Campo, J.M.; López-Gutiérrez, J.S.; Esteban, M.D. Review of coastal Land Reclamation situation in the World. *J. Coast. Res.* **2016**, *75*, 667–671. [CrossRef]
2. Huang, C.; Zhang, C.; Liu, Q.; Wang, Z.; Li, H.; Liu, G. Land reclamation and risk assessment in the coastal zone of China from 2000 to 2010. *Reg. Stud. Mar. Sci.* **2020**, *39*, 101422. [CrossRef]
3. Jiang, L.; Lin, H. Integrated analysis of SAR interferometric and geological data for investigating long-term reclamation settlement of Chek Lap Kok Airport, Hong Kong. *Eng. Geol.* **2010**, *110*, 77–92. [CrossRef]
4. Sengupta, D.; Chen, R.; Meadows, M.E. Building beyond land: An overview of coastal land reclamation in 16 global megacities. *Appl. Geogr.* **2018**, *90*, 229–238. [CrossRef]
5. Xu, N.; Gong, P. Significant coastline changes in China during 1991–2015 tracked by Landsat data. *Sci. Bull.* **2018**, *63*, 883–886. [CrossRef]
6. Tang, M.; Zhao, Q.; Pepe, A.; Devlin, A.T.; Falabella, F.; Yao, C.; Li, Z. Changes of Chinese Coastal Regions Induced by Land Reclamation as Revealed through TanDEM-X DEM and InSAR Analyses. *Remote Sens.* **2022**, *14*, 637. [CrossRef]
7. Wu, S.; Yang, Z.; Ding, X.; Zhang, B.; Zhang, L.; Lu, Z. Two decades of settlement of Hong Kong International Airport measured with multi-temporal InSAR. *Remote Sens. Environ.* **2020**, *248*, 111976. [CrossRef]
8. Liu, X.; Zhao, C.; Zhang, Q.; Yang, C.; Zhang, J. Characterizing and Monitoring Ground Settlement of Marine Reclamation Land of Xiamen New Airport, China with Sentinel-1 SAR Datasets. *Remote Sens.* **2019**, *11*, 585. [CrossRef]
9. Li, G.; Zhao, C.; Wang, B.; Liu, X.; Chen, H. Land Subsidence Monitoring and Dynamic Prediction of Reclaimed Islands with Multi-Temporal InSAR Techniques in Xiamen and Zhangzhou Cities, China. *Remote Sens.* **2022**, *14*, 2930. [CrossRef]
10. Shi, X.; Chen, C.; Dai, K.; Deng, J.; Wen, N.; Yin, Y.; Dong, X. Monitoring and Predicting the Subsidence of Dalian Jinzhou Bay International Airport, China by Integrating InSAR Observation and Terzaghi Consolidation Theory. *Remote Sens.* **2022**, *14*, 2332. [CrossRef]
11. Pepe, A.; Bonano, M.; Zhao, Q.; Yang, T.; Wang, H. The Use of C-/X-Band Time-Gapped SAR Data and Geotechnical Models for the Study of Shanghai's Ocean-Reclaimed Lands through the SBAS-DInSAR Technique. *Remote Sens.* **2016**, *8*, 911. [CrossRef]
12. Kim, S.-W.; Wdowinski, S.; Dixon, T.H.; Amelung, F.; Won, J.-S.; Kim, J.W. InSAR-based mapping of surface subsidence in Mokpo City, Korea, using JERS-1 and ENVISAT SAR data. *Earth Planets Space* **2008**, *60*, 453–461. [CrossRef]

13. Aimaiti, Y.; Yamazaki, F.; Liu, W. Multi-sensor InSAR analysis of progressive land subsidence over the coastal city of Urayasu, Japan. *Remote Sens.* **2018**, *10*, 1304. [CrossRef]
14. Aslan, G.; Cakır, Z.; Ergintav, S.; Lasserre, C.; Renard, F. Analysis of secular ground motions in Istanbul from a long-term InSAR time-series (1992–2017). *Remote Sens.* **2018**, *10*, 408. [CrossRef]
15. Poitevin, C.; Wöppelmann, G.; Raucoules, D.; Le Cozannet, G.; Marcos, M.; Testut, L. Vertical land motion and relative sea level changes along the coastline of Brest (France) from combined space-borne geodetic methods. *Remote Sens. Environ.* **2019**, *222*, 275–285. [CrossRef]
16. Jiang, L.; Lin, H.; Cheng, S. Monitoring and assessing reclamation settlement in coastal areas with advanced InSAR techniques: Macao city (China) case study. *Int. J. Remote Sens.* **2011**, *32*, 3565–3588. [CrossRef]
17. Shi, G.; Lin, H.; Bürgmann, R.; Ma, P.; Wang, J.; Liu, Y. Early soil consolidation from magnetic extensometers and full resolution SAR interferometry over highly decorrelated reclaimed lands. *Remote Sens. Environ.* **2019**, *231*, 111231. [CrossRef]
18. Xu, B.; Feng, G.; Li, Z.; Wang, Q.; Wang, C.; Xie, R. Coastal Subsidence Monitoring Associated with Land Reclamation Using the Point Target Based SBAS-InSAR Method: A Case Study of Shenzhen, China. *Remote Sens.* **2016**, *8*, 652. [CrossRef]
19. Chen, Y.; Yan, F.; Chen, J.; Fan, X. Detection Ground Deformation Characteristics of Reclamation Land with Time-Series Interferometric Synthetic Aperture Radar in Tianjin Binhai New Area, China. *Remote Sens.* **2023**, *15*, 5303. [CrossRef]
20. Bai, Z.; Wang, Y.; Li, M.; Sun, Y.; Zhang, X.; Wu, Y.; Li, Y.; Li, D. Land Subsidence in the Singapore Coastal Area with Long Time Series of TerraSAR-X SAR Data. *Remote Sens.* **2023**, *15*, 2415. [CrossRef]
21. Yu, Q.; Yan, X.; Wang, Q.; Yang, T.; Lu, W.; Yao, M.; Dong, J.; Zhan, J.; Huang, X.; Niu, C.; et al. A Spatial-Scale Evaluation of Soil Consolidation Concerning Land Subsidence and Integrated Mechanism Analysis at Macro-, and Micro-Scale: A Case Study in Chongming East Shoal Reclamation Area, Shanghai, China. *Remote Sens.* **2021**, *13*, 2418. [CrossRef]
22. Yang, M.; Yang, T.; Zhang, L.; Lin, J.; Qin, X.; Liao, M. Spatio-Temporal Characterization of a Reclamation Settlement in the Shanghai Coastal Area with Time Series Analyses of X-, C-, and L-Band SAR Datasets. *Remote Sens.* **2018**, *10*, 329. [CrossRef]
23. Biggs, J.; Wright, T.J. How satellite InSAR has grown from opportunistic science to routine monitoring over the last decade. *Nat. Commun.* **2020**, *11*, 3863. [CrossRef] [PubMed]
24. Wang, B.; Zhang, Q.; Zhao, C.; Pepe, A.; Niu, Y. Near Real-Time InSAR Deformation Time Series Estimation With Modified Kalman Filter and Sequential Least Squares. *IEEE J. Sel. Top. Appl. Earth Obs. Remote Sens.* **2022**, *15*, 2437–2448. [CrossRef]
25. Ferretti, A.; Prati, C.; Rocca, F. Permanent scatterers in SAR interferometry. *IEEE Trans. Geosci. Remote Sens.* **2001**, *39*, 8–20. [CrossRef]
26. Werner, C.; Wegmüller, U.; Strozzi, T.; Wiesmann, A. Interferometric point target analysis for deformation mapping. In Proceedings of the IEEE International Geoscience and Remote Sensing Symposium, Toulouse, France, 21–25 July 2003; Volume 7, pp. 4362–4364. [CrossRef]
27. Hooper, A.; Zebker, H.; Segall, P.; Kampes, B. A new method for measuring deformation on volcanoes and other natural terrains using InSAR persistent scatterers. *Geophys. Res. Lett.* **2004**, *31*, L23611. [CrossRef]
28. Costantini, M.; Falco, S.; Malvarosa, F.; Minati, F.; Trillo, F.; Vecchioli, F. Persistent scatterer pair interferometry: Approach and application to COSMO-SkyMed SAR Data. *IEEE J. Sel. Top. Appl. Earth Obs. Remote Sens.* **2014**, *7*, 2869–2879. [CrossRef]
29. Berardino, P.; Fornaro, G.; Lanari, R.; Sansosti, E. A new algorithm for surface deformation monitoring based on small baseline differential SAR interferograms. *IEEE Trans. Geosci. Remote Sens.* **2002**, *40*, 2375–2383. [CrossRef]
30. Ferretti, A.; Fumagalli, A.; Novali, F.; Prati, C.; Rocca, F.; Rucci, A. A new algorithm for processing interferometric data-stacks: SqueeSAR. *IEEE Trans. Geosci. Remote Sens.* **2011**, *49*, 3460–3470. [CrossRef]
31. Guarnieri, M.; Tebaldini, S. On the Exploitation of Target Statistics for SAR Interferometry Applications. *IEEE Trans. Geosci. Remote Sens.* **2008**, *46*, 3436–3443. [CrossRef]
32. Fornaro, G.; Verde, S.; Reale, D.; Pauciullo, A. CAESAR: An Approach Based on Covariance Matrix Decomposition to Improve Multibaseline–Multitemporal Interferometric SAR Processing. *IEEE Trans. Geosci. Remote Sens.* **2015**, *53*, 2050–2065. [CrossRef]
33. Lv, X.; Yazıcı, B.; Zeghal, M.; Bennett, V.; Abdoun, T. Joint-Scatterer Processing for Time-Series InSAR. *IEEE Trans. Geosci. Remote Sens.* **2014**, *52*, 7205–7221. [CrossRef]
34. Wang, B.; Zhao, C.; Zhang, Q.; Liu, X.; Lu, Z.; Liu, C.; Zhang, J. Sequential DS-ISBAS InSAR Deformation Parameter Dynamic Estimation and Quality Evaluation. *Remote Sens.* **2023**, *15*, 2097. [CrossRef]
35. Shi, G.; Ma, P.; Lin, H.; Huang, B.; Zhang, B.; Liu, Y. Potential of Using Phase Correlation in Distributed Scatterer InSAR Applied to Built Scenarios. *Remote Sens.* **2020**, *12*, 686. [CrossRef]
36. Pepe, A.; Yang, Y.; Manzo, M.; Lanari, R. Improved EMCF-SBAS processing chain based on advanced techniques for the noise-filtering and selection of small baseline multi-look DInSAR interferograms. *IEEE Trans. Geosci. Remote Sens.* **2015**, *53*, 4394–4417. [CrossRef]
37. Liu, J.; Hu, J.; Bürgmann, R.; Li, Z.; Sun, Q.; Ma, Z. A Strain-Model Based InSAR Time Series Method and Its Application to The Geysers Geothermal Field, California. *J. Geophys. Res. Solid Earth* **2021**, *126*, e2021JB021939. [CrossRef]
38. Osmanoğlu, B.; Sunar, F.; Wdowinski, S.; Cabral-Cano, E. Time series analysis of InSAR data: Methods and trends. *ISPRS J. Photogramm. Remote Sens.* **2016**, *115*, 90–102. [CrossRef]
39. Minh, D.H.T.; Hanssen, R.; Rocca, F. Radar interferometry: 20 years of development in time series techniques and future perspectives. *Remote Sens.* **2020**, *12*, 1364. [CrossRef]

40. Xue, F.; Lv, X.; Dou, F.; Yun, Y. A review of time-series interferometric SAR techniques: A tutorial for surface deformation analysis. *IEEE Geosci. Remote Sens. Mag.* **2020**, *8*, 22–42. [CrossRef]
41. Minh, D.H.T.; Tebaldini, S. Interferometric phase linking: Algorithm, application, and perspective. *IEEE Geosci. Remote Sens. Mag.* **2023**, *11*, 46–62. [CrossRef]
42. Galve, J.P.; Pérez-Peña, J.V.; Azañón, J.M.; Closson, D.; Calò, F.; Reyes-Carmona, C.; Jabaloy, A.; Ruano, P.; Mateos, R.M.; Notti, D.; et al. Evaluation of the SBAS InSAR Service of the European Space Agency’s Geohazard Exploitation Platform (GEP). *Remote Sens.* **2017**, *9*, 1291. [CrossRef]
43. Ma, P.; Lin, H.; Wang, W.; Yu, H.; Chen, F.; Jiang, L.; Zhou, L.; Zhang, Z.; Shi, G.; Wang, J. Toward Fine Surveillance: A review of multitemporal interferometric synthetic aperture radar for infrastructure health monitoring. *IEEE Geosci. Remote Sens. Mag.* **2021**, *10*, 207–230. [CrossRef]
44. Chang, L.; Dollevoet, R.P.B.J.; Hanssen, R.F. Nationwide railway monitoring using satellite SAR interferometry. *IEEE J. Sel. Top. Appl. Earth Obs. Remote Sens.* **2016**, *10*, 596–604. [CrossRef]
45. Zhang, Z.; Lin, H.; Wang, M.; Liu, X.; Chen, Q.; Wang, C.; Zhang, H. A review of satellite synthetic aperture radar interferometry applications in permafrost regions: Current status, challenges, and trends. *IEEE Geosci. Remote Sens. Mag.* **2022**, *10*, 93–114. [CrossRef]
46. Lazecky, M.; Hlavacova, I.; Bakon, M.; Sousa, J.J.; Perissin, D.; Patricio, G. Bridge displacements monitoring using space-borne X-band SAR interferometry. *IEEE J. Sel. Top. Appl. Earth Obs. Remote Sens.* **2016**, *10*, 205–210. [CrossRef]
47. Wang, B.; Li, W.; Zhao, C.; Zhang, Q.; Li, G.; Liu, X.; Yan, B.; Cai, X.; Zhang, J.; Zheng, S. L^2-Norm Quasi 3-D Phase Unwrapping Assisted Multitemporal InSAR Deformation Dynamic Monitoring for the Cross-Sea Bridge. *IEEE J. Sel. Top. Appl. Earth Obs. Remote Sens.* **2024**, *17*, 18926–18938. [CrossRef]
48. Wang, B.; Zhang, Q.; Pepe, A.; Mastro, P.; Zhao, C.; Lu, Z.; Zhu, W.; Yang, C.; Zhang, J. Analysis of Groundwater Depletion/Inflation and Freeze–Thaw Cycles in the Northern Urumqi Region with the SBAS Technique and an Adjusted Network of Interferograms. *Remote Sens.* **2021**, *13*, 2144. [CrossRef]
49. Pang, Z.; Jin, Q.; Fan, P.; Jiang, W.; Lv, J.; Zhang, P.; Cui, X.; Zhao, C.; Zhang, Z. Deformation Monitoring and Analysis of Reservoir Dams Based on SBAS-InSAR Technology—Banqiao Reservoir. *Remote Sens.* **2023**, *15*, 3062. [CrossRef]
50. Wang, B.; Zhao, C.; Zhang, Q.; Lu, Z.; Li, Z.; Liu, Y. Sequential estimation of dynamic deformation parameters for SBAS-InSAR. *IEEE Geosci. Remote Sens. Lett.* **2019**, *17*, 1017–1021. [CrossRef]
51. Dalaison, M.; Jolivet, R. A Kalman filter time series analysis method for InSAR. *J. Geophys. Res. Solid Earth* **2020**, *125*, e2019JB019150. [CrossRef]
52. Ma, Z.; Liu, J.; Aoki, Y.; Wei, S.; Liu, X.; Cui, Y.; Hu, J.; Zhou, C.; Qin, S.; Huang, T.; et al. Towards big SAR data era: An efficient Sentinel-1 Near-Real-Time InSAR processing workflow with an emphasis on co-registration and phase unwrapping. *ISPRS J. Photogramm. Remote Sens.* **2022**, *188*, 286–300. [CrossRef]
53. Cai, J.; Liu, G.; Jia, H.; Zhang, B.; Wu, R.; Fu, Y.; Xiang, W.; Mao, W.; Wang, X.; Zhang, R. A new algorithm for landslide dynamic monitoring with high temporal resolution by Kalman filter integration of multiplatform time-series InSAR processing. *Int. J. Appl. Earth Obs. Geoinf.* **2022**, *110*, 102812. [CrossRef]
54. Liu, J.; Hu, J.; Li, Z.; Zhang, L.; Sun, Q.; Zhu, J.; Wu, L. Dynamically estimating deformations with wrapped InSAR based on sequential adjustment. *J. Geodesy* **2023**, *97*, 49. [CrossRef]
55. Zhao, Q.; Pepe, A.; Gao, W.; Lu, Z.; Bonano, M.; He, M.L.; Wang, J.; Tang, X. A DInSAR investigation of the ground settlement time evolution of ocean-reclaimed lands in Shanghai. *IEEE J. Sel. Top. Appl. Earth Obs. Remote Sens.* **2015**, *8*, 1763–1781. [CrossRef]
56. Park, S.; Hong, S. Nonlinear Modeling of Subsidence From a Decade of InSAR Time Series. *Geophys. Res. Lett.* **2021**, *48*, 2020GL090970. [CrossRef]
57. Xiong, Z.; Deng, K.; Feng, G.; Miao, L.; Li, K.; He, C.; He, Y. Settlement Prediction of Reclaimed Coastal Airports with InSAR Observation: A Case Study of the Xiamen Xiang'an International Airport, China. *Remote Sens.* **2022**, *14*, 3081. [CrossRef]
58. Kim, S.; Wdowinski, S.; Dixon, T.H.; Amelung, F.; Kim, J.W.; Won, J. Measurements and predictions of subsidence induced by soil consolidation using persistent scatterer InSAR and a hyperbolic model. *Geophys. Res. Lett.* **2010**, *37*, L05304. [CrossRef]
59. Chen, Y.; He, Y.; Zhang, L.; Chen, Y.; Pu, H.; Chen, B.; Gao, L. Prediction of InSAR deformation time-series using a long short-term memory neural network. *Int. J. Remote Sens.* **2021**, *42*, 6919–6942. [CrossRef]
60. Hill, P.; Biggs, J.; Ponce-López, V.; Bull, D. Time-series prediction approaches to forecasting deformation in Sentinel-1 INSAR data. *J. Geophys. Res. Solid Earth* **2021**, *126*, e2020JB020176. [CrossRef]
61. Chen, J. Application of concrete four legged hollow blocks in the reclamation project of Funing Bay in Xiapu County. *Water Resour. Technol.* **2015**, *2*, 40–42. (In Chinese)
62. Goldstein, R.M.; Werner, C.L. Radar interferogram filtering for geophysical applications. *Geophys. Res. Lett.* **1998**, *25*, 4035–4038. [CrossRef]
63. Wang, B.-H.; Zhao, C.-Y.; Liu, Y.-Y. An improved SAR interferogram denoising method based on principal component analysis and the Goldstein filter. *Remote Sens. Lett.* **2017**, *9*, 81–90. [CrossRef]
64. Hooper, A. A multi-temporal InSAR method incorporating both persistent scatterer and small baseline approaches. *Geophys. Res. Lett.* **2008**, *35*, L16302. [CrossRef]
65. Li, W.; Zhao, C.; Wang, B.; Zhang, Q. L^1-norm sparse 2-D phase unwrapping algorithm based on reliable redundant network. *IEEE Geosci. Remote Sens. Lett.* **2020**, *19*, 1–5. [CrossRef]

66. Ma, Z.-F.; Jiang, M.; Khoshmanesh, M.; Cheng, X. Time series phase unwrapping based on graph theory and compressed sensing. *IEEE Trans. Geosci. Remote Sens.* **2021**, *60*, 1–12. [CrossRef]
67. Wang, B.; Zhao, C.; Zhang, Q.; Yang, C.; Li, W.; Li, G.; Kang, Y.; Zheng, S. SAR Interferometry Infrastructure Deformation Monitoring by the Number of Redundant Observations Optimizes Phase Unwrapping Networks. *IEEE J. Sel. Top. Appl. Earth Obs. Remote Sens.* **2023**, *16*, 7201–7212. [CrossRef]
68. Zhang, L.; Ding, X.; Lu, Z. Modeling PSInSAR time series without phase unwrapping. *IEEE Trans. Geosci. Remote Sens.* **2010**, *49*, 547–556. [CrossRef]
69. Shanker, A.P.; Zebker, H. Edgelist phase unwrapping algorithm for time series InSAR analysis. *J. Opt. Soc. Am. A* **2010**, *27*, 605–612. [CrossRef]
70. Pepe, A.; Lanari, R. On the extension of the minimum cost flow algorithm for phase unwrapping of multitemporal differential SAR interferograms. *IEEE Trans. Geosci. Remote Sens.* **2006**, *44*, 2374–2383. [CrossRef]
71. Tan, T.; Inoue, T.; Lee, S. Hyperbolic method for consolidation analysis. *J. Geotech. Eng.* **1991**, *117*, 1723–1737. [CrossRef]
72. Yang, P.; Tang, Y.; Zhou, N.; Wang, J. Consolidation settlement of Shanghai dredger fill under self-weight using centrifuge modeling test. *J. Cent. South Univ. Technol.* **2008**, *39*, 862–866. (In Chinese)